Cycloidal Magnetic Order Promoted by Labile Mixed Anionic Paths in M 2 (SeO 3)F 2 (M = Mn 2+ , Ni 2+)

Tianyu Zhu, Olivier Mentré, Haoming Yang, Yong Jin, Xinan Zhang, Ángel Arévalo-López, Clemens Ritter, Kwang-Yong Choi, Minfeng Lü

Cycloidal magnetic order promoted by labile mixed anionic paths in $M_2(SeO_3)F_2$ ($M=Mn^{2+}$, Ni^{2+})

Tianyu Zhu,[a] Olivier Mentré,[b,*] Haoming Yang,[a] Yong Jin,[a] Xinan Zhang,[a] Ángel M. Arévalo-López,[b] Clemens Ritter,[c] Kwang-Yong Choi,[d] and Minfeng Lü,[a,*]

[a] *School of Environmental & Chemical Engineering, Jiangsu University of Science and Technology, Zhenjiang 212003, Jiangsu, Perople's Republic of China*

[b] *Université Lille Nord de France, UMR 8181 CNRS, Unité de Catalyse et de Chimie du Solide (UCCS USTL), F-59655 Villeneuve d'Ascq, France.*

[c] *Institut Laue-Langevin, Avenue des Martyrs 71, Grenoble Cedex, France*

[d] *Department of Physics, Chung-Ang University, 84 Heukseok-ro, Dongjak-gu, Seoul 06974, Republic of Korea*

Keywords: *transition metal oxide fluorides, building units, hydrothermal, single-crystal X-ray diffraction, magnetic structure*

Abstract

Two $M_2(SeO_3)F_2$ fluoro-selenites (M = Mn^{2+}, Ni^{2+}) have been synthesized using optimized hydrothermal reactions. Their 3D framework consists of 1D-$[MO_2F_2]^{4-}$chains of edge-sharing octahedra with a rare topology of O-O and F-F alternating μ_2 bridges. The inter-chain corner sharing connections are assisted by the mixed O *vs.* F anionic nature and develop a complex set of M-X-M super-exchanges calculated by LDA+U. Their interplay induce prominent in-chain antiferromagnetic frustration while the interchain exchanges are responsible for the cycloidal magnetic structure observed below T_N ~21.5 K in the Ni^{2+} case. For comparison the Mn^{2+} compound develops a nearly collinear spin (canted) ordering below T_N ~26 K with ferromagnetic chain-units.

1. Introduction

Compounds with multiple anions have received great interests from the inorganic solid-state chemists due to hetero-anionic characteristics adding new dimensions on the electronic structure, which may support physical phenomena inaccessible to a single-anion analog, including competition between labile magnetic exchanges.[1] Recently, multiple anions ideas have been extended to the oxy-halide system of M–L–O–X (M = metal cation, L =p-block lone-pair elements such as Te^{4+}, Se^{4+}, X =halide anion. It is common that the role of lone pair cations on selenites as chemical scissors help to form low-dimensional framework materials. Halide insertion leads to two categories: the larger halide ions ($Cl^-$and Br^-) are inclined to generate extended non-bonding regions when interacting with lone-pair elements so that the two-dimensional (2D) structure is often adopted, see $Cu_5(SeO_3)_4Cl_2$.[2] On the other hand, the smaller fluoride anion may act as a bridging species between transition metal cations forming there by sizeable dimensionalities in phases such as the 1D-$Fe(SeO_3)F$[3], or the 3D-$M_2(SeO_3)F_2$ (M = Co, Cu).[4,5]Here, the contrasting magnetic exchanges mediated by O^{2-} *vs.* F^- may procure a playground for destabilizing the standard collinear spin order into exotic ones, and provide a nice platform for spin-induced multiferroicity.[6] Only few examples of selenium-oxofluorides have been reported due to hard control of the reactive fluorine ions[7-9] using HF (or else) as a dual mineralizer and strong acid, suitable for the formation of metal ions. In fact, reacting SeO_2, metal halide and HF acid is a suitable strategy to grow single crystals of $M_2(SeO_3)F_2$ (M = Co, Cu).[4,5] The realization of polycrystalline mixed $(Mn,Zn)_2(SeO_3)F_2$ by fine adjustment of the pH environment using NH_4OH was achieved, but the crystal growth was hampered by the reduction of Se(IV) to Se(0) above 120°C [10] which remains a chemical challenge. Similarly, powdered samples of $M_2(SeO_3)F_2$ (M = Mn, Co, Ni) have first been achieved via hydrothermal techniques. The crystal structures of $M_2(SeO_3)F_2$ (M = Mn, Ni) were then solved by powder diffraction until the single crystals of isostructural $Co_2(SeO_3)F_2$ were obtained by chemical transport reactions.[11] In this work, we report the preparation, single crystal growth and structures of the $M_2(SeO_3)F_2$ (M = Mn, Ni) analogues. Although several $M^{2+}{}_2(SeO_3)F_2$ have been reported, their full

magnetic characterization is original. We probe here versatile magnetic exchanges scaled by M-X-M paths, which return a nearly-collinear (M = Mn) versus cycloidal (M = Ni) magnetic structures analyzed by means of *ab*-initio calculations and neutron diffraction.

2. Experimental section

2.1 Synthesis

Powdered $M_2(SeO_3)F_2$ (M = Mn, Co, Ni) compounds can be achieved by HF as a mineralizer under hydrothermal conditions. However, an environment having too low pH value is not suitable for the formation of single crystals. We introduced hydrazine to enhance the pH of the hydrothermal solutions and to obtain single crystals of $Mn_2(SeO_3)F_2$. To recover single crystals of $Ni_2(SeO_3)F_2$, we introduce KOH to adjust the pH of the hydrothermal solutions. Our $Mn_2SeO_3F_2$ (**I**) and $Ni_2SeO_3F_2$ (**II**) compounds were obtained as single crystals and powdered samples, detailed in Supplementary Materials (SM).

2.2 Characterization

The SCXRD data of all the investigated samples have been collected using a Bruker SMART APEX II diffractometer with a 1K CCD area detector and monochromated Mo Kα radiation (λ = 0.71073 Å) at room temperature. To acquire the data, a narrow-frame method was used with scan widths of 0.30° in ω and an exposing time of 10 s/frame. Integration of the obtained data has been performed via the program SAINT .[12] Absorption corrections have been carried out by the multi-scan method using the program SADABS.[13] The crystallographic data for all the reported compounds are listed in Tables 1. Deposition number CCDC 2046139, 2046140 for $Mn_2SeO_3F_2$ and $Ni_2SeO_3F_2$, respectively. The refined anisotropic displacement parameters and atomic coordinates are summarized in the SM. The pertinent distances and angles are listed in Table S3,S6.

PXRD patterns were collected using a Bruker D8 Advance X-ray powder diffractometer with CuKα radiation (λ = 1.54056 Å, 40 kV/40 mA). The XRD powder patterns shown in Figure 1, match well the calculated patterns using the model obtained from the single crystal data reported.

Energy-dispersive analysis by X-ray (EDAX) of the isolated blue crystals was carried out using a Phenom ProX desktop analyser. Infrared spectra for the reported materials were recorded on a Varian 670-IR FTIR spectrometer. As the synthesis route can introduce hydroxyl groups instead of fluorine ions,

the presence of fluorine was verified by EDX analysis (Figure S1, S2) and the absence of OH groups around 3500 cm^{-1} by I.R spectroscopy (Figure S3). X-ray photoelectron spectroscopy (XPS) measurements were performed using a Thermo Scientific K-Alpha^{+} instrument. Thermogravimetric analysis (TGA) was performed using a thermal gravimetric analyser (Model: TGA5500, TA Instruments). Detailed experimental information provided in SM (Figure S4- S7).

The DC magnetic susceptibilities for polycrystalline $Mn_2SeO_3F_2$ and $Ni_2SeO_3F_2$ were measured by a commercial Quantum Design Physical Properties Measurement System (PPMS). Zero-field cooled (ZFC) and field cooled (FC) data were recorded within the temperature range of 2-400 K with an external field of 1000 Oe. Isothermal magnetization curve was collected in a field range of -9 to 9 T.

The specific heat measurement was collected with the heat capacity option of a physical properties measurement system (PPMS-9, Quantum Design).

Neutron powder diffraction (NPD) data were collected on the high intensity powder diffractometer D20 at the Institut Laue Langevin (ILL), Grenoble, France. Long acquisitions of 5 hours were taken at 1.5 K and 30 K for $Ni_2SeO_3F_2$. The thermal dependence between 2 K and 30 K was studied using shorter runs of 15 min taking spectra about every 0.7 K. This thermo-diffractogram confirmed that all magnetic Bragg peaks appear at the same temperature and show a similar temperature dependence indicating thereby the presence of a single magnetic propagation vector. High resolution data on the Ni-compound were taken at 2 K on D2B, as well at the ILL, with $\lambda = 1.594$ Å and confirmed the persistence of the *Pnma* structure. $Mn_2SeO_3F_2$ was measured at 1.5 K and 30 K on D20 using 30 min runs. NPD patterns were refined by the Rietveld method using the program FULLPROF.[14]

2.3 DFT Calculations

Density functional theory (DFT) band structure calculations were performed using the full-potential local-orbital scheme (FPLO9.00-33). [15]Applying the local density approximation (LDA + U, U = 3.6) with the exchange-correlation potential by Perdew and Wang.[16] using Vienna *ab initio* simulation package (VASP)[17] with the basis set of projected augmented waves;[18] we mapped the total energies for a number of collinear spin configurations into a classical Heisenberg model to yield individual exchange

couplings for U = 4.6eV and the effective on-site exchange interaction J_{eff} = 1eV. The set of magnetic configurations used to deduce the main exchange values are given in Figure S13 together with the details of their energies.

Table 1. Crystal data, measurement parameters and structural refinement parameters of $M_2SeO_3F_2$ (M = Mn, and Ni) at room temperature.

	$Mn_2SeO_3F_2$	$Ni_2SeO_3F_2$
Molar weight (g/mol)	274.8	282.3
Symmetry	orthorhombic	orthorhombic
Space group	*P nma*	*P nma*
a (Å)	7.4958(3)	7.1727(5)
b (Å)	10.3382(4)	9.9377(7)
c (Å)	5.4717(2)	5.2364(4)
V (Å^3)	424.02(3)	373.25(5)
μ (mm^{-1})	14.481	19.773
R(int) (%)	4.34	7.74
indep all (I > 3σ(I))	554	488
indep obsd (I > 3σ(I))	452	359
Number of refined	40	40
$R(F)^a$[$I > 3\sigma(I)$/all data,	3.27/4.09	3.36/5.22
$R_w (F^2)^b$ [$I > 3\sigma(I)$/all	4.38/4.45	3.64/3.85
Max/Min residual	0.86/-2.00	1.00/-1.11

$^aR = \sum \| F_o| - |F_o \| / \sum |F_o|$, $^bR_w = [\sum w(|F_o^2| - |F_c^2|)^2 / \sum w|F_o^2|^2]^{1/2}]$

3. Results and discussion

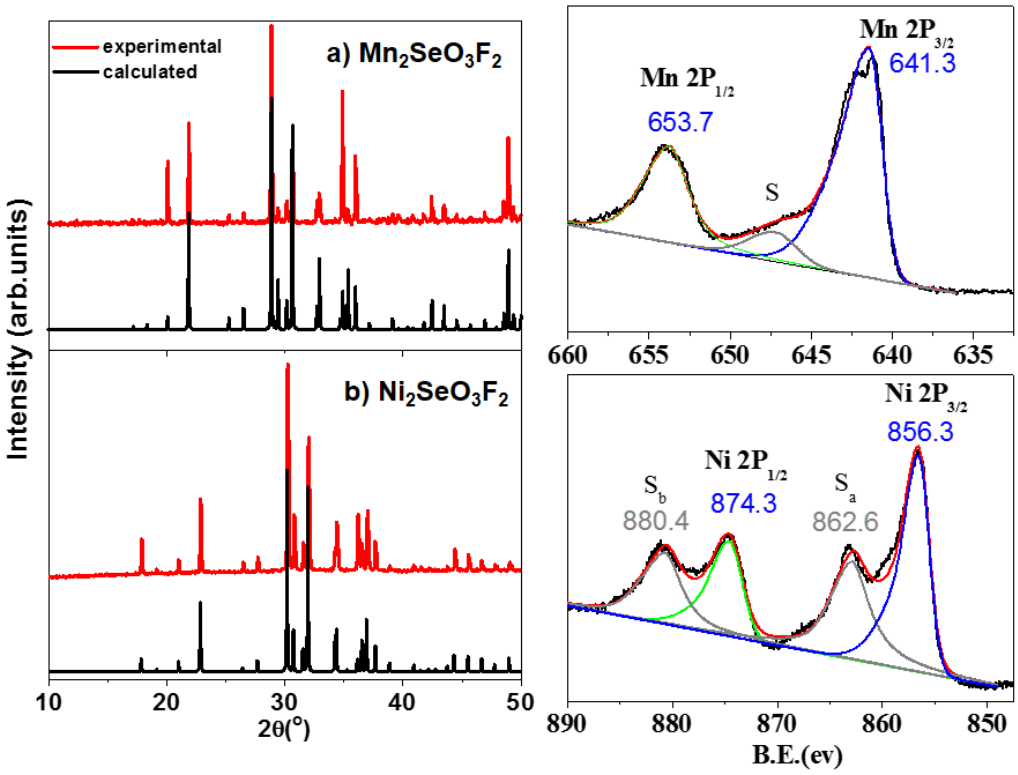

Figure 1:X-ray powder patterns of the experimental (red) and calculation from the single crystal XRD data (black), Mn/Ni *2p* XPS data for (a) $Mn_2SeO_3F_2$ and (b) $Ni_2SeO_3F_2$.

Both reported compounds $Mn_2(SeO_3)F_2$ (a = 7.4958(3)Å, b = 10.3382(4)Å, c = 5.4717(2)Å, Z = 4, R_F = 3.27%) and $Ni_2(SeO_3)F_2$ (a = 7.1727(5)Å, b = 9.9377(7)Å, c = 5.2364(4)Å, Z = 4, R_F =3.36%) crystallize in the orthorhombic space group, *Pnma* and are isomorphous with the $M_2(XO)_3F_2$, (M = Co, Cu, Mn and X = Te, Se).[4,5,10] Note that our single crystal XRD data allows for a more accurate structural model than reported for the Mn and Ni compounds necessary for the DFT calculations initiated later. A significant but isotropic contraction of all lattice parameters by ~5% occurs for $Ni_2(SeO_3)F_2$ related to the Mn^{2+} *vs.* Ni^{2+} relative ionic radii, which highlights the three-dimensional (3D) character of the framework.

The Mn/Ni coordination is a distorted MO_3F_3 octahedron, with distances given in SM (Table S3 and S6), all oxygen being shared by $(SeO_3)_2$ trigonal pyramidal groups, where stereochemically active selenium lone pair completes a distorted tetrahedra. As described before,[5] the crystal structure of $M_2SeO_3F_2$ is composed of $[MO_3F_3]$ octahedra and SeO_3 trigonal pyramids. The isostructural description is established on $Mn_2SeO_3F_2$, as detailed in SM (Figure S8). Rather than the description of the dense 3D-packing used for the parent $Co_2(TeO)_3F_2$,[5] we will refer here to the assembly of 1D-subunits already

pointed out in the (Zn,Mn) case,[10] much better suited to the decoding of the magnetic properties detailed below. Here one should focus on the most-dense 1D-zigzag chains formed by edge sharing along the *c*-axis of alternatively O-O and F-F μ_2 bridges, creating a rare situation reported only for $Na_2Fe(PO_4)F$[19] and $Fe(SeO_3)F$[3] to the best of our knowledge. The individual edge-sharing chains are highlighted on the Figure 2a-b for clarity. These chains share all their O and F corners apart the edge-sharing O_2 bridges with surrounding chains, leaving a dense 3D-lattice projected in the (*a*,*b*) on Figure 2b. The bases of the chains are parallel along the *a*-axis and tilted by ~110° leading to nearly triangular channels occupied by the Se^{4+} ions. Bond valence sum calculations [20] for Mn^{2+} (ΣS_i =1.98(1)) and Ni^{2+}(ΣS_i=1.96(1)) confirm divalent metal states, tetravalent Se^{4+}cations, and allow the clear distinction of O^{2-} against F^- sites, see Table S7.

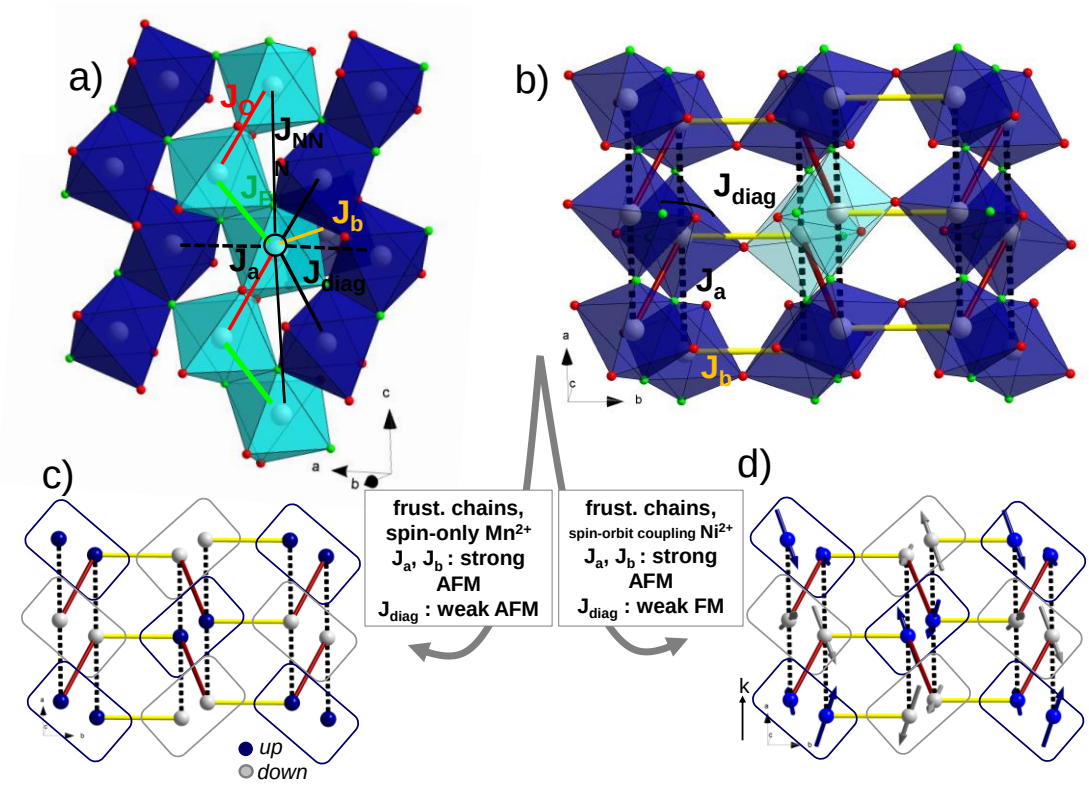

Figure 2: $M_2(SeO_3)F_2$ crystal structure and labels of the main magnetic exchanges. a,b) inter-chain connections for two projections in the (*a*,*c*) and (*a*,*b*) planes. O and F are in red and green respectively. The pale blue units allow to distinguish an edge-sharing chain from its (dark blue) neighbors. c-d) projected magnetic structure for c) M= Mn, d) M = Ni where the rectangles show the projected edge-sharing chains.

The Mn(II) and Ni(II) and hetero-coordination were further certified by XPS spectroscopy. The shape and position of the Mn *2p* core level indicate the divalent Mn oxidation state also characterized by

its intense "shake-up" satellite, approximately 6 eV below the main 2p peaks, shown in Figure 1a. The binding energy of the Mn$2p_{3/2}$ peak centered at 641.3 eV is consistent with the ones found for MnO (640.9 eV[21]) and MnF_2 (642.4 eV[22]). Since there is one crystallographically unique Mn atom, the $2p_{3/2}$ peak centered at 641.3 eV is intermediate between the one for MnF_2 (642.4 eV) and another for MnO (640.9 eV) supporting the mixed anionic Mn coordination.

The valence state of the Mn(II) ion was further confirmed by the magnitude of the exchange splitting of the core-level spectra of Mn *3s*. More specifically, one peak splits into two due to the exchange interaction between the Mn *3s* and Mn *3d* electrons.[22] The Mn *3s* splitting value for **I** is approximately 6.3 eV, as shown in Figure S5, which is consistent with the value of 6.3 eV for MnF_2 [21] and 5.8 eV for MnO.[23]

The XPS Ni2p patterns of **II** are also shown in Figure 1b and the typical Ni$2p_{3/2}$, Ni$2p_{1/2}$ and satellite (s) peaks are indicated. Similarly, the most intense peak, around 856.3 eV, is intermediate between the one for NiF_2 (858.1 eV) and another for NiO (853.8 eV),[24] in good agreement with Ni^{2+} in its NiO_3F_3 octahedron.

The Magnetic susceptibility of $Mn_2SeO_3F_2$ is similar to what reported in reference 10. In few words, it shows a ZFC/FC divergence below T_N = 26.1(1) K. The Curie−Weiss fit above 100 K, results in a Curie-Weiss temperature (θ_{CW}) = −71.0(1) K and μ_{eff} = 5.88(2) μ_B per Mn^{2+} (see Figure S9, against 6.06μ_B / Mn^{2+} in reference 10), close to the spin-only value of 5.92 μ_B (S = 5/2, L = 0, g = 2), similar to other Mn^{2+} fluorophosphates such as $(NH_4)Mn_3(PO_3F)_2(PO_2F_2)F_2$[7], $Ba_2Mn_2(PO_3F)F_6$.[25] Figure 3b shows the isothermal magnetization M(H) at various temperatures which reaches M_{9T}~1.17 μ_B/Mn^{2+} at 2.4 K. The aligned moment for our sample is also higher than what reported for polycrystals (M_{12T}~0.84 μ_B/Mn^{2+}).[10] A clear hysteresis with a coercive field of ~ 0.2 T and a remnant moment of ~0.012 μ_B/Mn^{2+} is assigned to a canting angle at zero field of $\sin^{-1}(0.012/5)$ ° = 0.13° assuming 5μ_B per Mn^{2+}. This phenomenon is further enhanced above the field-induced metamagnetic transition centered at μ_0H = 4 T. Here a canting angle of θ = 2.87° at 9 T can be estimated after subtracting the linear AFM M(H) component. Given the absence of symmetry centers in the main inter- and intra-chains super-exchange paths (see below), Dzyaloshinki-Moriya effects are plausible to explain such spin canted phenomenon.

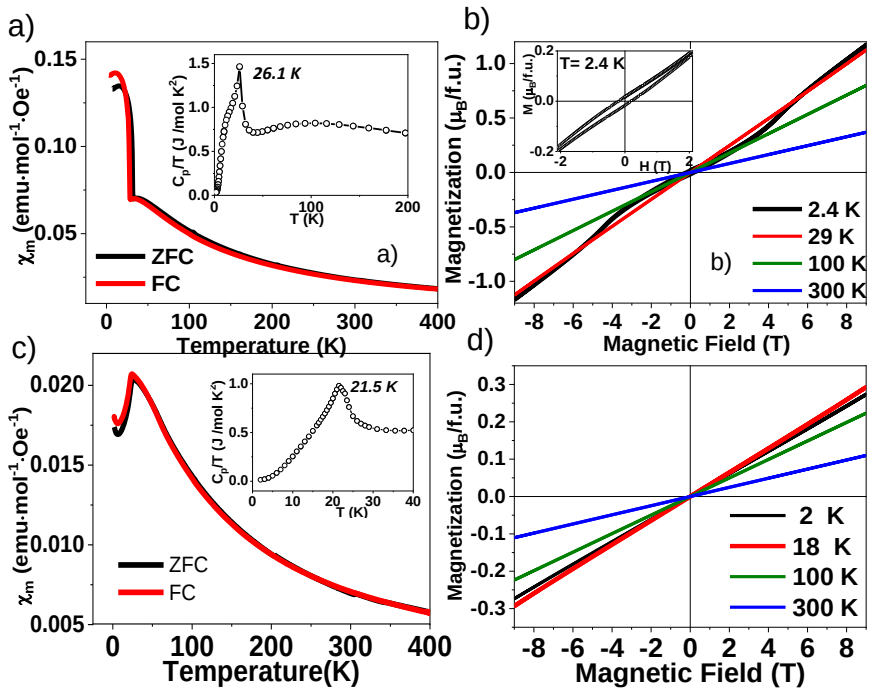

Figure 3: FC and ZFC curves of (a) $Mn_2SeO_3F_2$ and (c)$Ni_2SeO_3F_2$, the insets shows the specific heat divided by temperature $C_p(T)/T$ between 2 and 300 K. Field dependence of magnetization taken between 2.4 K and 300 K of (b) $Mn_2SeO_3F_2$ and (d)$Ni_2SeO_3F_2$. The inset shows an enlarged view of low-field range at 2.4 K.

Figure 3c shows no significant ZFC/FC divergence for $Ni_2SeO_3F_2$, thus the onset of AFM ordering occurs below T_N=21.7(1) K. This is supported also by the λ-shaped anomaly observed in specific heat measurements, see the inset of Figure 3c. The Curie-Weiss fit above T_N returns θ_{CW} = -100.9(1) K, μ_{eff} = 3.37(1) μ_B per Ni^{2+} (see Figure S11). The negative θ_{CW} suggests predominant antiferromagnetic interactions between the Ni^{2+} ions. μ_{eff} is higher than the spin-only value of 2.82 μ_B, indicating a significant orbital contribution of Ni^{2+} in an octahedral environment, similar to $Ni_3(TeO_3)(SO_4)(OH)_2{\cdot}2H_2O$. [26] $M(H)$ for $Ni_2SeO_3F_2$, is plotted in Figure 3d. It increases linearly with increasing field and reaches M_{9T} = 0.13 μ_B/Ni^{2+} at 2 K confirming robust AFM.

The magnetic structure of $Mn_2(SeO_3)F_2$ was solved and refined using powder neutron diffraction (PND) data collected at 1.5K on the D20 diffractometer (λ=2.41 Å) at the Institut Laue langevin (ILL), Grenoble, France. Magnetic contributions appear below T_N on nuclear contributions according to the propagation vector k = [0 0 0], the main ones violating the *Pnma* extinctions. The magnetic symmetry analysis using *Basireps*[14] indicates a decomposition of the Γ magnetic representation into 8 irreducible representations of dimension1, contained 3 times each in Γmagn= $3\Gamma_1 + 3\Gamma_2 + 3\Gamma_3 + 3\Gamma_4 + 3\Gamma_5 + 3\Gamma_6$

$+3\Gamma_7 + 3\Gamma_8$. Only the representation Γ5 leads to a good agreement between experimental and calculated intensities, using the Mz contribution only (Mx, My=0), see Table 2. The refinement of the magnetic contribution pattern ($T_{1.5K}$-T_{50K}) yields R_{Magn} =12.7% and M_{Mn2+}= 4.34(1) μ_B. The magnetic structure consists of ferromagnetic collinear edge-sharing chains running along z, AFM coupled by corner sharing along x and y axes.

Table 2. Basis vector Sx,Sy, Sz and the associated irreducible presentation Γi associated to the equivalent positions for the magnetic structures of $M_2(SeO_3)F_2$ (M= Mn, and Ni) compounds.

	M=Mn (M_z = 4.34(1) μB)			**M=Ni** (M_x =-1.82(5), M_y=0.6(1), M_z=-1.77(5) μ_B)	
coordinates	Sz : Γ_5,z		Sx : Γ_3,x	Sy : Γ_4,y	Sz : Γ_2,z
	real		*imaginary*	*imaginary*	*real*
x,y,z	+mz	Orbit 1	0	0	+mz
x+ ½ ,-y+½ ,-z+ ½	+mz		-mx.sinkπ	-my.sinkπ	+mz.sinkπ
x+½ ,y,-z+½	-mz		+mx.coskπ	-my.coskπ	-mz.coskπ
x,-y+½ ,z	-mz		0	0	-mz
-x+½ ,-y ,z+½	-mz	Orbit 2	0	0	+mz
-x,y+½ ,-z	-mz		-mx.sinkπ	-my.sinkπ	+mz.sinkπ
-x,-y,-z	+mz		+mx.coskπ	-my.coskπ	-mz.coskπ
-x+½ ,y+ ½ ,z+½	+mz		0	0	-mz

The situation is far different dealing with $Ni_2(SeO_3)F_2$ where combined high-resolution D1B and high intensity D20 data were necessary to identify an incommensurate propagation vector refined to k = [0.303(1) 0 0] , which curiously remains temperature independent below T_N, see Figure S12. The group theory analysis splits Ni into two orbits (x,y,z) and (-x+½ ,-y ,z+½), sharing the same decomposition of magnetic representations $\Gamma_{magn} = 3\Gamma_1 + 3\Gamma_2 + 3\Gamma_3 + 3\Gamma_4$. The combination of imaginary and real part of the three later has been used, which results are given in Table 2. Then the magnetic structure could be treated either by a sinusoidal or a cycloidal spin ordering indistinguishable by PND. The sinusoidal wave returns a modulated spin amplitude, with unrealistic maximal values of 2.6 μ_B for Ni^{2+} S = 1. Thus, we adopt the cycloidal description. The best refinement resulted in R_{Magn} = 16.8%. The spin order consists of magnetic moments rotating mainly in the (*ac*) plane, along the incommensurate *a*-axis. The phase between the two orbits was refined to 0.40(1)π. However due to the non-zero imaginary M_y components (see Table 2), the spin precession follows a complex-cycloidal sequence along the incommensurate *a*-axis, sketched in Figure 4e. Here, the cycloidal spin component within the (*ac*) plane is described by $M_{x,max}$ =1.82 μ_B and $M_{z,max}$ = 1.77 μ_B , but oscillates around the equatorial (*ac*) plane by the sinusoidal M_y

component scaled by $M_{y,max}$ = 0.6 μ_B. The final refinement of this model, leaving unconstrained M_x, M_y and M_z as given in Table 2, gives a nearly constant Ni^{2+}moment of average 1.85 μ_B value.

Frustration indexes of $|\theta_{CW}|/T_N$ = 2.7 and 4.6 for $Mn_2(SeO_3)F_2$ and $Ni_2(SeO_3)F_2$ respectively are in accordance with their refined magnetic structures. For the Ni compound for instance, one would expect next neighbour (NN) AFM edge-sharing chains due to super-exchange paths with M-X-M angle > 100° but frustration triggers a cycloidal magnetic structure. Dealing with $Ni^{2+}(d^8)$ against $Mn^{2+}(d^5)$ cations the Goodenough-Kanamori rules may predict the main signs of super-exchanges, at least for ideal 180° and 90° M-X-M interactions, but for intermediate values ab-initio calculations generally prevail. Clearly for S=5/2 spins, the chains are expected AFM for any angles and also by direct M-M t_{2g} overlap. In contrast for Ni^{2+} S=1, interactions depend on the angle, while direct t_{2g}-t_{2g} are inefficient. [27]The main identified magnetic exchanges, listed in Table 3 and shown Figure 2, and show in the chains intermediate M-X-M angles around 102°. They have been calculated using LDA+U, after mapping the total energies for a number of collinear spin configurations onto a classical Heisenberg model to yield individual exchange couplings for U = 4.6eV [28] and the effective on-site exchange interaction J_{eff}= 1eV. The calculated exchange strengths are scaled by the d(Ni-Ni)<d(Mn-Mn) interatomic distances returning weakest J's for Mn^{2+}, but counter-balanced by the relative Ni^{2+}(S=1) *vs.* Mn^{2+} (S=5/2) spin values, such that they finally order magnetically at similar Néel temperatures, ie. T_N =21.5 K (Ni) vs. T_N=26.5 (Mn). Note that the set of calculated exchanges match rather well the Curie-Weiss temperature estimated in the mean field model $\theta_{CW} = (1/3)\Sigma_i S(S+1)(J_i/k_B)$ giving calculated/experimental values of-95/-71 K and -88/-101 K for the Mn and Ni compounds respectively.

Dealing with the M-O-M exchange interaction J_O across the super exchange (SE) O-O bridge are antiferromagnetic in all cases but also predominant over the J_F one in both compounds (J_O/J_F ~1.8) although the O electrons are covalently engaged in strong Se-O bonds, similarly to what is observed in $Fe(SeO_3)F$.[3] This superior magnetic connection is not only due to the scaling effect of the longer M-F over M-O bonds s, [29] but mainly stem from the O *vs.* F electronegativity contrast, which favour strongest electronic exchanges via oxygen media. Here, the weakest J's for the Mn^{2+} compound exclude a significant contribution of direct t_{2g}-t_{2g} exchanges via the shared edges expected AFM for Mn^{2+} (d^5) but inefficient for Ni^{2+} (d^8). However, the diagonal J_{NNN} (NNN:*next*-nearest *neighbour*) super-super exchange in the edge-sharing chains is significant and destabilizes the AFM chains through strongly

frustrated M_3 triangles along the zig-zag chains. In addition, between the chains, the influence of exchange interactions J's should be considered not only by its value but also according to its occurrence giving a key-role to the inter-chain J_a and J_b SE's. They dictate the observed magnetic structures as follows: In the Mn case, they are largely predominant (~ 2-3 x $J_{in\text{-}chain}$) and the magnetic structure respect the $J_{b>}$ J_b > J_{diag} interplay. It returns ferromagnetic edge-sharing chains but antiferromagnetically ordered between each other across the corner-sharing exchanges, see Figure 4a, 4b.

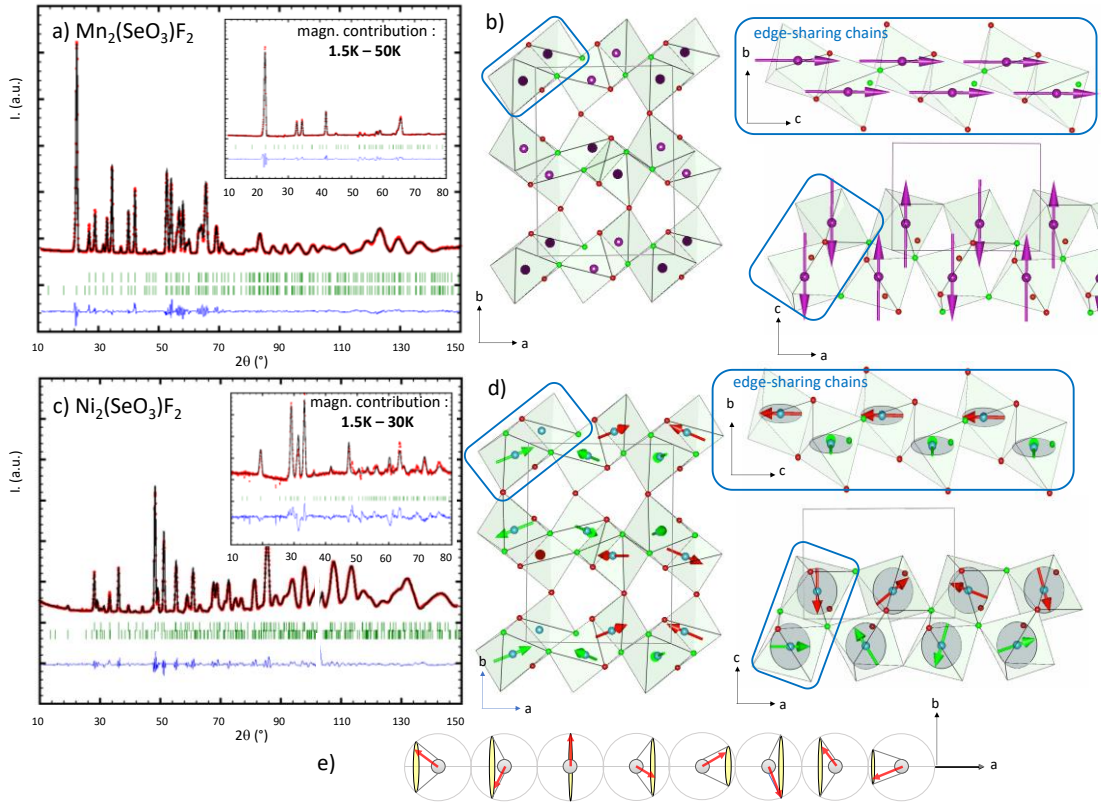

Figure 4: PND Rietveld refined patterns at 1.5 K (AFM-paramagnetic difference in the inset) and refined magnetic models for a-b) $Mn_2(SeO_3)F_2$ and c-d)$Ni_2(SeO_3)F_2$.e) Scheme of the magnetic cycloid along the *a*-axis in the latter.

Table 3. The magnetic exchange geometrical parameters for different exchange paths in $M_2(SeO_3)F_2$(M= Mn, and Ni). Interatomic distances , angles (SE) and dihedral angles(SSE) are given.

Compound	$Mn_2(SeO_3)F_2$,T_N= 26.1 K,θ_{CW} = -71.0(1) K	$Ni_2(SeO_3)F_2$, ,T_N= 21.7 K,θ_{CW} = - 100.9(1) K

Exchange type	Mn-Mn (Å)	Mn-X_{SE} (Å), X-X_{SSE}(Å) *	Mn-X-M_{SE} (°), Mn-X-X-Mn_{SSE}(°) *	J/K_b (K)	Ni-Ni (Å) ,X-X_{SSE}(Å) *	Ni-X (Å), Ni-X-X-Ni_{SSE}(°) *	Ni-X-Ni (°)	J/K_b (K)
1x J_O(M-O_2-M)	3.39	2.13, 2.24	101.8	2.74	3.16	2.02,2.06	101.4	24.26
1xJ_F (M-F_2-M)	3.38	2.15,2.15	103.7	1.53	3.17	2.05, 2.06	101.3	13.51
2x J_{NNN}(M-O-F-M) *	2.47	3.05,	74.5	3.02	5.22	2.80,	67.6	16.87
2x J_a (M-F-M)	3.75	2.11, 2.15	123.1	5.56	3.58	2.02, 2.04	123.9	25.56
1x J_b (M-O-M)	3.77	2.16, 2.16	121.9	9.72	3.75	2.09, 2.09	127.3	17.01
2x J_{diag}(M-F-M)	3.84	2.11, 2.15	128.8	1.51	3.68	2.01, 2.06	129.8	-3.37$_{FM}$

In addition, in this case the isotropic magnetic single ion Mn^{2+} (L=0) plays in favour of a collinear magnetic structure commensurate with the crystallographic axis. This is the case here with spins oriented along the *a*-axis which does not correspond to any local specific octahedral direction. On the opposite, in the anisotropic Ni^{2+} ions with significant spin-orbit coupling (SOC) (μ_{eff} = 3.37 μ_B), the orientation of the magnetic moments are ruled by local orbital overlap, sometimes more prompt for spin wave-like features in which the spin orientation is hold but its amplitude is modulated in the crystal. However, counter examples with rotating spins are common including the spiral spin order of Fe^{3+} (L=0) in $BiFeO_3$. In fact, the exact opposite situation compared to the title Mn/Ni tandem has been reported in $Sr(Mn,Co)Ge_2O_6$ with similar ferromagnetic zigzag chain with a collinear magnetic structure, [30] but for the Co^{2+} case (strong SOC) while the Mn^{2+} (isotropic spin) compound develops a cycloidal spin configuration and spin-induced multiferroicity. It follows that the relative J's interplay may by its own dictate the magnetic structure.[30] In $Ni_2(SeO_3)F_2$, the magnitudes of the interchain exchanges J_a , J_b are similar to those inside the edge sharing -chains, such that the frustration is destabilized into a cycloidal structure, keeping from site-to-site the main characteristic as for the Mn^{2+} case, see Figure 2d. In addition, the role of the weak ferromagnetic J_{diag} SSEs adds an extra degree of frustration in favor of the incommensurate magnetic period.

Summarising, $M_2(SeO_3)F_2$ (M = Mn^{2+}, Ni^{2+}),comprised of 1D-$[MO_2F_2]^{4-}$chains of edge-sharing octahedra with a rare topology of O-O and F-F alternating μ_2 bridges, were obtained as single crystals by an optimised hydrothermal route. Neutron diffraction experiments on powders indicate $Mn_2SeO_3F_2$ exhibits a canted AFM ordering below 26K with ferromagnetic chain-units. Here the AFM ordering between them relies on predominant inter-chain interactions. In the isostructural $Ni_2SeO_3F_2$, the frustration is increased due to inter and intra chain couplings of same order of magnitude promoting an incommensurate cycloidal magnetic structure below 21.5K. While, intuitively the significant SOC observed for Ni^{2+} may be a plausible crucial parameter in favour of the cycloidal state, the exact opposite situation found in recent pyroxene compounds $SrMGe_2O_6$ with M=Co and Mn [30] emphasizes the relevant role of the sensitive nature of the magnetic ground state in topologies with apparent dominating low-D units, but complex overall exchange interplay. Further pushing this analogy allows the anticipation of Type II multiferroicity, currently under test for $Ni_2(SeO_3)F_2$.

Supporting Information

Detailed experimental information, crystal data tables, magnetic structure and DFT calculation methods are provided as Supporting Information. This material is available free of charge via the Internet at http://pubs.acs.org.

AUTHOR INFORMATION

Corresponding Author

E-mail address: m.f.lv@hotmail.com (Minfeng Lü)

olivier.mentre@univ-lille.fr (Olivier Mentré)

ORCID[ID]

Minfeng Lü: 0000-0003-2576-3840

Clemens Ritter: 0000-0003-3674-3378

Angel M. Arévalo-López: 0000-0002-8745-4990

Notes

The authors declare no competing financial interests.

Acknowledgments

T. Z., H. Y., Y. J., X. Z., and M.L. acknowledge support from the National Natural Science Foundation of China (Award No.21671185). O.M., and A-M. A-L acknowledge support from the ANR (Grant ANR-16-CE08-0023) and the FEDER Région Hauts-de-France, they also acknowledge the ILL for the allocated beamtime (DOI 10.5291/ILL-DATA.EASY-654) and the ILL Instrument Control Service for their support before and during the experiment.Claire Minaud is also thanked for experimental help. Finally dealing with mixed anion compounds, the JSPS Core-to-Core Program (A) Advanced Research Networks (JPJSCCA20200004) is also acknowledged as a source of motivation.

References:

(1) Kageyama, H.; Hayashi, K.; Maeda, K.; Attfield, J. P.; Hiroi, Z.; Rondinelli, J. M.; Poeppelmeier, K. R. Expanding frontiers in materials chemistry and physics with multiple anions. *Nat. Commun.* **2018**, *9*, 772.

(2) Zhang, D.; Berger, H.; Kremer, R .K.; Wulferding, D.; Lemmens, P.; Johnsson, M. Synthesis, Crystal Structure, and Magnetic Properties of the Copper Selenite Chloride $Cu_5(SeO_3)_4Cl_2$. *Inorg. Chem.* **2010**, *49*, 9683-9688.

(3) Hu, S.; Johnsson, M.; Law, J. M.; Bettis, J. L.; Whangbo, M.-H.; Kremer, R. K. Crystal Structure and Magnetic Propertiesof $FeSeO_3F$—alternating Antiferromagnetic S = 5/2 Chains. *Inorg. Chem.* **2014**, *53*, 4250–4256.

(4) Hu, S.; Johnsson, M. Synthesis and crystal structure of two synthetic oxofluoride framework compounds–$Co_2TeO_3F_2$ and $Co_2SeO_3F_2$. *Dalton Trans.***2012**, *41*, 12786−12789.

(5) Mitoudi-Vagourdi, E.; Papawassiliou, W.; Mullner,S.; Jaworski, A.; Pell, A. J.; Lemmens, P.; Kremer, R. K.; Johnsson, M. Synthesis and Physical Properties of the Oxofluoride $Cu_2(SeO_3)F_2$. *Inorg. Chem.* **2018**, *57*, 4640-4648.

(6) Tokura, Y.; Sekiand, S.; Nagaosa, N. Multiferroics of spin origin. *Rep. Prog. Phys.* **2014**, *77*, 076501.

(7) Jiang, J.; Zhu, B.; Zhu, T.; Yang H.; Jin, Y.; Lü, M. Open-framework ammonium transition metal fluorophosphates with a Kagomé lattice network: synthesis, structure and magnetic properties. *Dalton Trans.* **2020**,*49*, 841-849.

(8) Jiang, J.; Lee, S.; Zhu, B.; Yu, Y.; Waerenborgh ,J. C.; Choi, K.-Y.; Lü, M. Variable Dimensionality, Valence, and Magnetism in Fluoride-Rich Iron Phosphates $Ba_xFe_x(PO_4)F_y$ ($1 \leqslant x \leqslant 3, 2 \leqslant y \leqslant 12$). *Inorg. Chem.* **2019**, *58*, 133-142.

(9) Lü, M.; Jiang, J.; Zhu, B.; Zhao, Y.; Zhu, T.; Yang, H.; Jin, Y.; Kabbour, H.; Choi, K.-Y.; Harrison, W. T. A. Lone-pair self-containment in pyritohedron-shaped closed cavities: optimized hydrothermal synthesis, structure, magnetism and lattice thermal conductivity of $Co_{15}F_2(TeO_3)_{14}$. *Dalton Trans.* **2020**, *49*, 2234-2243.

(10) Orive, J.; Balda, R.; Fernández, J.;Lezama, L.; Arriortua. M. I. Low temperature red luminescence of a fluorinated Mn-doped zinc selenite. *Dalton Trans.* **2013**, *42*, 12481-12494.

(11) Hu, S.*Transition metal oxofluorides comprising lone pair elements*; Doctoral Thesis 2014 Department of Materials and Environmental Chemistry Inorganic Chemistry Arrhenius Laboratory Stockholm University SE-10691 Stockholm Sweden Stockholm University: Stockholm, 2014.

(12) *SAINT: Area-Detector Integration Software*; Siemens Industrial Automation, Inc.: Madison, 1996.

(13) *SADABS: Area-Detector Absorption Correction*; Siemens Industrial Automation, Inc.: Madison, 1995.

(14) Rodriguez-Carvajal, J. Recent advances in magnetic structure determination by neutron powder diffraction.*Physica B.* **1993**, ***55***, 192.

(15) Koepernik,K.; Eschrig, H. Full-potential nonorthogonal local-orbital minimum-basis band-structure scheme. *Phys. Rev. B* **1999**, *59*, 1743.

(16) Perdew, J. P.; Wang, Y. Pair-distribution function and its coupling-constant average for the spin-polarized electron gas. *Phys. Rev. B* **1992**, *45*, 13244.

(17) Kresse, G.; Furthmüller, J. *Vienna Ab-initio Simulation Package (VASP)*; Institut für Materialphysik: Vienna, Austria, 2004.

(18) Kresse, G.; Furthmüller,J. Efficiency of ab-initio total energy calculations for metals and semiconductors using a plane-wave basis set. *Comput. Mater. Sci.* **1996**, *6*, 15; Efficient iterative schemes for ab initio total-energy calculations using a plane-wave basis set. *Phys. Rev. B* **1996**, *54*, 11169.

(19) Ellis, B. L.; M.Makahnouk, W. R.; Rowan-Weetaluktuk, W. N.; Ryan, D. H.; Nazar, L. F. Crystal Structure and Electrochemical Properties of A_2MPO_4F Fluorophosphates (A = Na, Li; M = Fe, Mn, Co, Ni). *Chem. Mater.***2010**, *22*, 1059-1070.

(20) Brese, N. E.; O'Keeffe, M. Bond-valence parameters for solids.*Acta Crystallogr.* **1991**, *B47*, 192–197.

(21) Nelson, A. J.; Reynolds, J. G.;Roos, J. W. Core-level satellites and outer core-level multiplet splitting in Mn model compounds. *J. Vac. Sci. Technol. A.* **2000**, *18*, 1072-1076.

(22) Carver, J. C.; Schweitzer, G. K.; Carlson, T. A. Use of X‐Ray photoelectron spectroscopy to study bonding in Cr, Mn, Fe, and Co compounds. *J. Chem. Phys.* **1972**, *57*, 973.

(23) Oku, M.; Hirokawa, K.; Ikeda, S. X-ray photoelectron spectroscopy of manganese-oxygen systems. *J. Electron Spectrosc. Relat. Phenom.* **1975**, *7*, 465.

(24) Biesinger,M. C. ; Lau, L. W. M. A. ; Gerson, R. ; Smart, R. St. C. The role of the Auger parameter in XPS studies of nickel metal,halides and oxides. *Phys. Chem. Chem. Phys.* **2012**, *14*, 2434–2442.

(25) Zhu, B.; Jiang, J.; Zhu, T.; Yang, H.; Jin, Y.; Choi, K.-Y.; Lü, M. Transition-Metal Monofluorophosphate $Ba_2M_2(PO_3F)F_6$ (M = Mn, Co, and Ni): Varied One-Dimensional Transition-Metal Chains and Antiferromagnetism. *Inorg. Chem.* **2020**, *59*, 3794-3804.

(26) Tang, Y.; Guo, W.; Zhang, S.; Yang, M.; He, Z. $M_3(TeO_3)(SO_4)(OH)_2{\cdot}2H_2O$ (M = Ni, Co): Two Novel Quasi-2D Layered Tellurite-Sulfate Compounds with a Distorted Striped Kagomé Lattice. *Cryst. Growth Des.* **2014**, *14*, 5206-5211.

(27) Goodenough, J. B. *Magnetism and the Chemical Bond*; Wiley, New York,1963.

(28) Trimarchi, G.; Wang, Z.; Zunger, A. Polymorphous band structure model of gapping in the antiferromagnetic and paramagnetic phases of the Mott insulators MnO, FeO, CoO, and NiO. *Phys. Rev. B.* **2018**, *97*, 035107.

(29) Pedersen, K. S.; Sigrist, M. Weihe, H.; Bond, A. D.; Thuesen, C. A.; Simonse, K. P.; Birk, T.; Mutka, H.; Barra, A.-L.; Bendix, J. Magnetic Interactions through Fluoride: Magnetic and Spectroscopic Characterization of Discrete, Linearly Bridged $[Mn^{III}_2(\mu\text{-}F)F_4(Me_3tacn)_2](PF_6)$. *Inorg. Chem.* **2014**, *53*, 5013-5019.

(30) Ding, L.; Colin, C. V.; Darie, C.; Bordet, P. $SrMGe_2O_6$ (M= Mn, Co): a family of pyroxene compounds displaying multiferroicity.*J. Mater. Chem. C.* **2016**, *4*, 4236-4245.

Highlights:

$Mn_2SeO_3F_2$ containing alternating O_2 and F_2 bridges along 1D-chains show versatile magnetic ordering (canted collinear/Mn against incommensurate cycloidal/Ni) understood by means of inter-chain exchanges calculations.